2007

Local Heat Transfer Coefficients Induced by Piezoelectrically Actuated Vibrating Cantilevers

M. Kimber

S V. Garimella
Purdue University, sureshg@purdue.edu

A. Raman
Purdue University

Follow this and additional works at: http://docs.lib.purdue.edu/coolingpubs

Local Heat Transfer Coefficients Induced by Piezoelectrically Actuated Vibrating Cantilevers

Mark Kimber

Suresh V. Garimella[1]
e-mail: sureshg@purdue.edu

Arvind Raman

NSF Cooling Technologies Research Center,
School of Mechanical Engineering,
Purdue University,
585 Purdue Mall,
West Lafayette, IN 47907-2088

Piezoelectric fans have been shown to provide substantial enhancements in heat transfer over natural convection while consuming very little power. These devices consist of a piezoelectric material attached to a flexible cantilever beam. When driven at resonance, large oscillations at the cantilever tip cause fluid motion, which in turn results in improved heat transfer rates. In this study, the local heat transfer coefficients induced by piezoelectric fans are determined experimentally for a fan vibrating close to an electrically heated stainless steel foil, and the entire temperature field is observed by means of an infrared camera. Four vibration amplitudes ranging from 6.35 to 10 mm are considered, with the distance from the heat source to the fan tip chosen to vary from 0.01 to 2.0 times the amplitude. The two-dimensional contours of the local heat transfer coefficient transition from a lobed shape at small gaps to an almost circular shape at intermediate gaps. At larger gaps, the heat transfer coefficient distribution becomes elliptical in shape. Correlations developed with appropriate Reynolds and Nusselt number definitions describe the area-averaged thermal performance with a maximum error of less than 12%. [DOI: 10.1115/1.2740655]

Keywords: local heat transfer, piezoelectric fan, electronics cooling, vibrating cantilever, heat transfer enhancement

Introduction

A piezoelectric fan consists of a piezoelectric material bonded to a flexible cantilever blade. An alternating input signal causes the piezoelectric material to contract and expand, generating bending moments on the blade at the edges of the piezoelectric material. These moments produce oscillations at the free end of the cantilever blade, and when driven at the resonance frequency of the structure, the oscillations become large and serve to agitate and move the surrounding fluid, which enhances heat transfer when compared to natural convection alone. These fans consume very little power and can be built to meet different geometric constraints for many applications while remaining relatively noiseless. Because of this, piezoelectric fans offer an attractive electronics thermal management solution.

Various aspects of piezoelectric fans have been studied in the literature. A detailed analysis of the two-dimensional flow field generated from a vibrating cantilever beam was presented by Kim et al. [1]. Vortices were observed to be shed each time the beam passed the position of zero displacement, i.e., at twice the vibration frequency. The maximum fluid velocity was found to be roughly four times that of the maximum tip velocity. Açıkalın et al. [2] developed analytical models describing the streaming flow induced by a single vibrating piezoelectric fan and found good qualitative agreement between the predicted flow patterns and experimental visualizations for small displacements. Feasibility studies for implementing piezoelectric fans in electronic systems were conducted by Açıkalın et al. [3] and Wait et al. [4], where piezoelectric fans were placed within a laptop to further enhance the heat transfer performance of the rotary fan by increasing the fluid mixing in stagnant regions normally not accessed by the rotary fan. A simulated cell phone enclosure was also considered for which enhancements over natural convection were quan-

tified for various piezoelectric fan orientations. Numerical modeling of the fluid flow and heat transfer induced by a piezoelectric fan has also been conducted [5]. The flow field generated by these fans was found to be extremely complex and highly dependent on the distance from fan tip to the heat source, as well as other boundary conditions.

The two-dimensional flow field generated from two flexible cantilevers was analyzed experimentally by Ihara and Watanabe [6]. They investigated the behavior for in-phase and out-of-phase vibration at three different pitches. The cantilevers were sandwiched between two large plates, thereby approximating a two-dimensional flow field. The results were compared to the flow field generated by a single cantilever in the same experimental setup, and the volumetric flow rate for in-phase vibration of two cantilevers was found to be approximately double that of a single cantilever. Mass transfer experiments on a vertical surface targeted by two piezoelectric fan blades were conducted by Schmidt [7] using the naphthalene sublimation technique. The fan blades vibrated out of phase and the fan pitch was kept constant. Power-law correlations were found to reasonably describe both maximum and surface-averaged Sherwood numbers for three separate distances from the vertical surface. In each case the Sherwood numbers formed contours symmetric about the midpoint of fan separation. Fluidic coupling between multiple fans was observed by Kimber et al. [8], who showed that as two fans operate in close proximity, their vibration characteristics are modified. Under in-phase vibration, this can lead to a decrease in viscous drag seen by the fans and yield a further increase in vibration amplitude; this in turn provides enhancement in the overall heat transfer. They considered multiple fan pitches for both in-phase and out-of-phase vibration, and discovered an optimal fan pitch to maximize the average heat transfer rates; this optimum was roughly equal to the vibration amplitude.

Bürmann et al. [9], Basak et al. [10], and Kim et al. [11] have explored the structural dynamics of these devices, particularly with regard to optimization by considering the mechanical work and maximum tip displacement that can be achieved, as functions of the geometric and material properties of the piezoelectric fan.
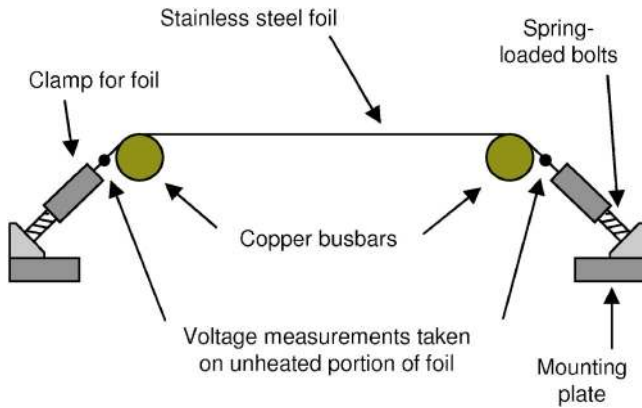

Fig. 1 Schematic diagram of constant heat flux surface

Açıkalın et al. [5] investigated a single piezoelectric fan vibrating near a small heat source to determine the conditions under which the average heat transfer could be optimized. The factors considered were fan length, vibration amplitude, frequency offset and distance from the heat source.

The present work aims at describing the behavior of the local heat transfer coefficients of flows generated from a piezoelectric fan. A detailed treatment of this topic is essential to providing insight into the underlying phenomena related to these fans, as well as to help in their implementation into practical designs.

Experimental Setup and Procedures

Details of the experimental setup for measurement of local temperature distributions are first presented, followed by methods for calculating the heat transfer coefficients and a description of the parameters of interest.

Experimental Setup. The experimental setup includes a flat, constant heat flux surface mounted in a vertical position on an optical table. Both sides of the heat source are exposed to ambient conditions. A piezoelectric fan is mounted normal to the heat source on one side (the "front" side) on a linear stage enabling precise positioning of the distance from the heat source. Only vibration in the horizontal direction is considered, and a laser displacement sensor (Keyence LK-G157) is positioned to capture the vibration signal of the fan tip. The heat source is coated on both sides with a thin layer of Krylon #1602 black paint having a known emissivity of 0.95 [12], and a thermal image of the back side of the heat source (i.e., side opposite from the fan) is captured with an infrared camera (ThermaCAM Merlin). A plexiglass enclosure is built around the entire setup to isolate it from extraneous flows within the room.

The constant-flux heat source design is similar to those in Refs. [13,14], and a schematic illustration is shown in Fig. 1. It consists of an electrically heated thin stainless steel (Type 302) foil stretched over two 25.4 mm diameter copper rods acting as busbar terminals. The foil is 0.051 mm thick and 101.6 mm wide. A power supply provides the required potential drop across the copper rods. The copper rods are located a distance of 203.2 mm apart, thereby providing a heated surface area of 101.6 mm × 203.2 mm. The unheated portions of the foil extending beyond the copper rods are clamped between two pieces of steel held together by three bolts traveling through holes in both the clamp and foil. The clamped foil is then attached to a mounting plate by means of spring-loaded bolts. The bolts are tightened to eliminate any slack at room temperature, and as the foil is heated, the springs accommodate the thermal expansion to maintain the heated foil in tension. A thick (25.4 mm) plexiglass frame holds the heater assembly together and also provides electrical isolation

between the two extreme sides of the heater.

Due to the absence of an interface material or mechanical bond between the copper and stainless steel foil, the electrical contact resistance proved to be appreciable compared to the electrical resistance of the heated foil ($\sim$0.03 Ω). To account for this, voltage measurements are taken directly on the unheated ends of the foil as shown in Fig. 1, whereas the current input from the power supply is simultaneously monitored. Because current only flows through the portion of the foil between the busbars, no voltage drop occurs along the unheated length. Measuring voltage using contacts in the unheated portion avoids the problem of local cooling that would be caused if the probes were in contact with the heated portion of the foil. This method of voltage and current measurement adequately describes the power input to the heated portion of the foil without disturbing the heat transfer behavior of the heated surface.

Although the resistivity of stainless steel is temperature dependent (temperature coefficient of resistance measured to be 1.6 $\times 10^{-4}$ $\Omega/°C$), measurements of the voltage at multiple points along the length of the heater revealed that this has no effect on the linearity of the voltage drop across the heater. As the voltage drop across the heater and the current supplied to the heater are used to calculate the local heat flux, any nominal change in resistance is accounted for, and will not have an adverse effect on the accuracy of the local heat flux estimation.

Lateral conduction effects leading to thermal smearing are estimated by analyzing the respective magnitudes of each mode of heat transfer (radiation and convective heat losses to both sides of the foil, and conduction heat transfer through the foil) compared to the overall heat generated at a specified location. Such an estimation revealed the heat transfer by lateral conduction to be less than 2% of the heat generated; smearing by lateral conduction is therefore negligible.

As the thermal conductivity of the copper busbars is much larger than that of the stainless steel, the copper can act as a local heat sink. This localized cooling effect is confined to a region close to the busbars; therefore, all the heat transfer results are reported for the portion of the heated foil sufficiently remote from the busbars. A span of foil 25.4 mm in length adjacent to each copper rod is excluded from the analysis, leaving a heated surface area of 101.6 mm × 152.4 mm that is considered in the measurements.

Local Heat Transfer Calculations. The electrically generated heat flux (q''_{gen}) is uniform across the entire heated surface, and is computed according to

$$q''_{gen} = \frac{V_s I_s}{A_{heat}} \tag{1}$$

A local flux balance is used to determine the convection coefficient due to the piezoelectric fans, as illustrated in Fig. 2. Radiation losses (q''_{rad}) on both sides of the heater are computed from the measured temperature field as

$$q''_{rad} = \varepsilon \sigma (T_s^4 - T_\infty^4) \tag{2}$$

and the heat loss by natural convection (q''_{nc}) on the side opposite the fans is found by first performing detailed experiments to determine the local natural convection coefficients (h_{nc}) and using them in:

$$q''_{nc} = h_{nc}(T_s - T_\infty) \tag{3}$$

The remaining component of the heat generated is dissipated as q''_{mix} by mixed convection with contributions from both forced convection (due to the piezoelectric fan) and natural convection. The relationship in such a regime can be expressed according to [15]:
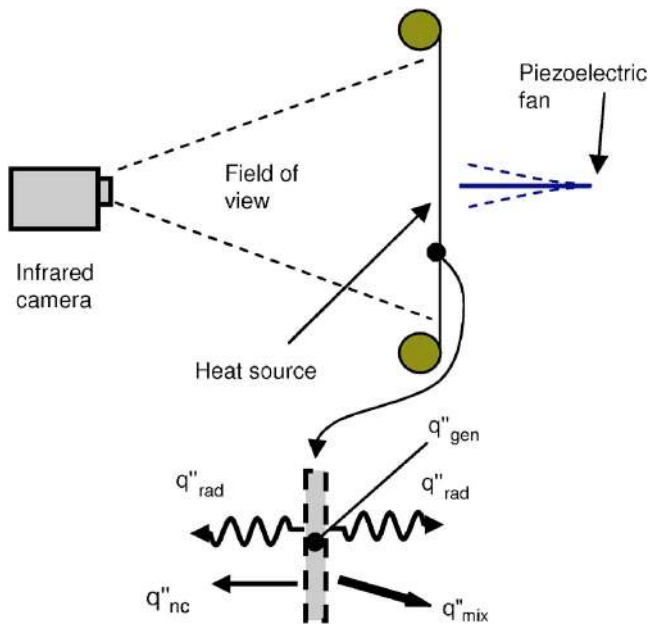
Fig. 2 Flux balance on foil (neglecting lateral conduction)

$$\mathrm{Nu}_{\mathrm{mix}}^3 = \mathrm{Nu}_{\mathrm{pz}}^3 + \mathrm{Nu}_{\mathrm{nc}}^3 \qquad (4)$$

Taking each of these Nusselt numbers to be based on the same length scale, the convection coefficient attributed to the piezoelectric fan (h_{pz}) can be extracted according to

$$h_{\mathrm{pz}} = (h_{\mathrm{mix}}^3 - h_{\mathrm{nc}}^3)^{1/3} \qquad (5)$$

where h_{mix} is directly found from:

$$h_{\mathrm{mix}} = \frac{q''_{\mathrm{gen}} - 2q''_{\mathrm{rad}} - q''_{\mathrm{nc}}}{T_s - T_\infty} \qquad (6)$$

The convection coefficients reported in the results below exclusively represent the forced convective contribution from the piezoelectric fan (i.e., h_{pz}).

Experimental Parameters. The commercially available fans used in these experiments are made from a flexible mylar blade. As shown in Fig. 3, the overall fan length (L) is 64.0 mm, width
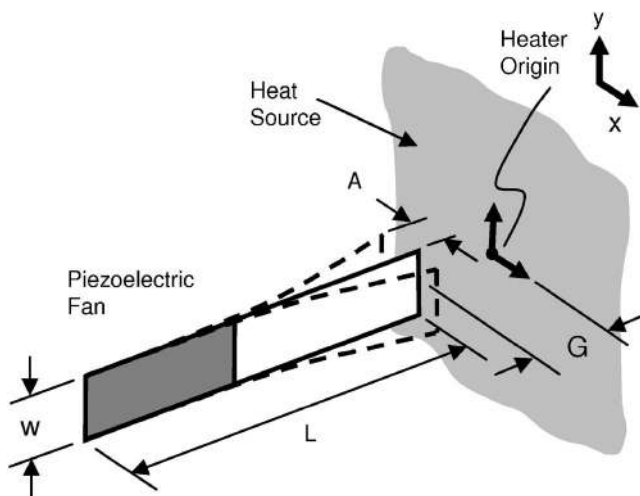

Fig. 3 Geometric parameters of fan: length (L) and width (w). Also shown are the parameters varied throughout experiments: vibration amplitude (A) and gap distance from heat source (G).

Table 1 Variable parameter values in the experiments

Parameter	Units	Values tested
Amplitude (A)	mm	6.35, 7.5, 8.5, 10
G/A	—	0.01–2.0 (21 values)

(w) is 12.7 mm, and the fundamental resonance frequency of the fan is 60 Hz. Also illustrated in Fig. 3 are the two parameters varied during the heat transfer experiments: vibration amplitude (A), which is half the peak-to-peak amplitude, and gap distance (G) from fan tip to heater surface. Four different amplitudes are investigated ranging from 6.35 to 10 mm, where the lower number is half the fan width ($w/2$) and the higher number is the amplitude corresponding to the maximum input to the piezoelectric element below the depoling voltage (i.e., the voltage that causes a permanent change in polarization). It has previously been shown by Kimber et al. [16] that for small amplitudes and large gaps, the behavior is fundamentally different when compared to that seen at the opposite extreme (i.e., large amplitude and small gap). In light of this fact, the nondimensional quantity G/A is used to describe the gap distance. The range of this parameter and the four amplitudes considered within the experiments are given in Table 1. There are 21 different gaps for each amplitude, yielding a total of 84 experiments. The excitation frequency for each experiment is 60 Hz and the input signal magnitude was adjusted to obtain the desired vibration amplitude for each experiment; it may be noted that due to fluidic damping, a larger input voltage is required for fans vibrating close to a surface (small gaps). The power required to drive the fans varies across the experiments as a result, and ranges from 10 to 40 mW depending on the vibration amplitude. The tests thus compare performance for specified amplitude rather than for a given power consumption.

The uncertainty associated with the determination of convection coefficients has two primary contributions: Errors in temperature measurement and estimation of the generated heat flux. The uncertainty in the latter is caused by the resolution of the voltage and current measurements as well as uncertainties in the measurement of the heat source dimensions. The largest source of error is in the temperature measurement, which affects the estimation of the radiation flux, natural convection flux, and the mixed regime flux. The experimental error induced by the infrared camera was quantified using a blackbody emitter (SBIR 2004) with a temperature control within ±0.02°C. This revealed a temperature measurement error of ±1°C over a temperature range of 20–80°C. For the experiments, the heat input to the heater was chosen such that during forced convection, the minimum temperature observed was approximately 40°C, causing a worst-case error of ±2.5% in the temperature reading on the heated surface. Based on this analysis, the estimated uncertainty in forced convection coefficients is approximately ±8%.

Experimental Results

Accurate determination of the forced convection coefficient (h_{pz}) requires a thorough analysis of the setup under natural convection conditions. Natural convection heat transfer coefficients are first characterized followed by the forced convection coefficients.

Natural Convection. The temperature field in a representative natural convection experiment is shown in Fig. 4 where temperatures range from approximately 50°C at the leading edge ($y = -50.8$ mm) to 66°C at the top ($y = 50.8$ mm) for a power input to the heater of 16 W. The near-horizontal nature of the isotherms is consistent with the behavior expected of natural convection on a heated vertical surface [17]. The temperature profile under such conditions is predicted to increase with vertical position to the 1/5
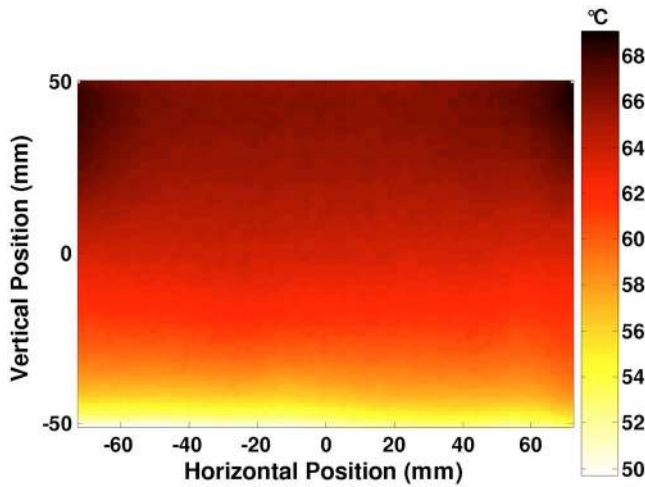
Fig. 4 Natural convection temperature distribution

Fig. 6 Experimental convection coefficient (h_{pz}) for A =10 mm (top row), A=8.5 mm (second row), A=7.5 mm (third row), and A=6.35 mm (bottom row). Each column represents a different gap corresponding to G/A=0.01, 0.5, and 2.0. The heater size shown is 101.6 mm×152.4 mm.

power. The measured temperature profile is shown in Fig. 5 to conform to this dependence very well. The measured average convection coefficient is 5.3 W/m² K, which is also comparable with predicted value of 6.4 W/m² K from the Vliet and Ross correlation [17].

The left and right edges near the top of the heater show slightly higher temperatures (by ≈3 °C) than at the center of the top edge. This is attributed to the disruption of the natural convection boundary layers by the copper rods, which is more pronounced as the boundary layers grow towards the top of the heated surface. However, the central area of the heater is isolated from these effects, and provides a robust experimental vehicle for the characterization of piezoelectric fan heat transfer.

Forced Convection. Local forced convection coefficient (h_{pz}) maps are presented in Fig. 6; the same scale is used in all the images to enable direct qualitative and quantitative comparison between the different cases. Twelve unique cases are shown (out of the total of 84 experiments conducted), with rows and columns representing changes in amplitude and gap, respectively. For each amplitude, results are shown at G/A values at which the temperature contours show a significant change in distribution. The fan is located in the middle of the heater and the vibration envelope is superimposed on each image. The solid vertical line in the center
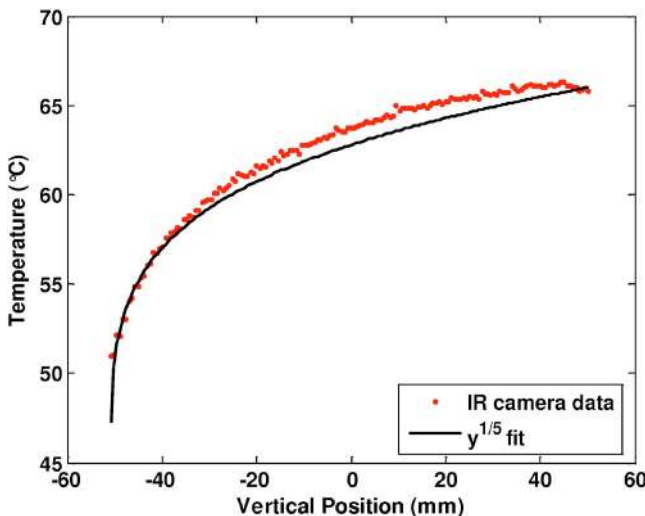

Fig. 5 Natural convection temperature profile in the vertical direction at the heat source center, x=0 mm

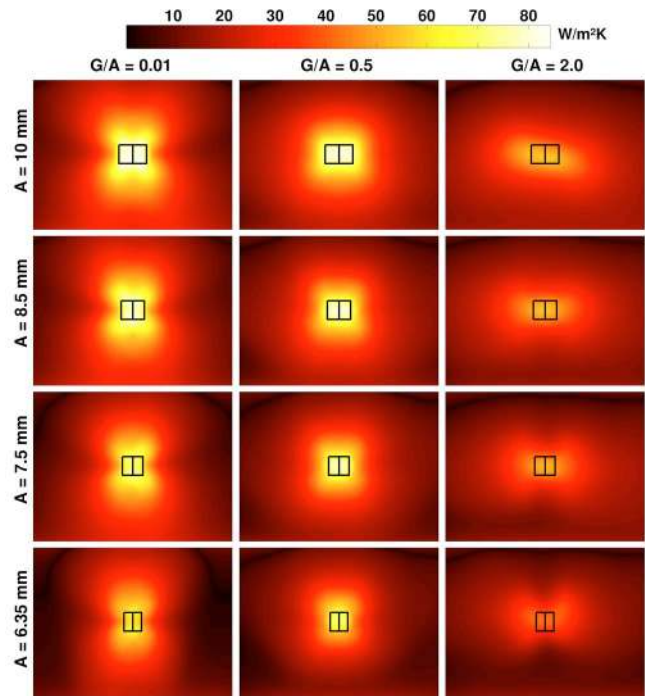represents the fan at its zero (undisplaced) position with the remaining lines illustrating the extent of the vibration envelope, whose overall dimensions are twice the vibration amplitude in the horizontal direction, and equal to the width of the fan in the vertical direction. The heater size shown is 101.6 mm × 152.4 mm. The largest amplitude considered (A=10 mm) is shown along the top row of Fig. 6 for gaps of G/A=0.01, 0.5, and 2.0. A lobed pattern is generated when the fan vibrates close to the surface, and these lobes appear to be symmetric in both the vertical and horizontal directions, suggesting that the fluid agitation is roughly similar in the vibration direction and its orthogonal direction. This behavior transitions to a nearly circular (or rounded square) shape for the intermediate gaps, while the largest gap results in a distinctly different distribution of heat transfer coefficients. The fluid agitation at this gap is less influential in the vertical direction (orthogonal to the direction of vibration), yielding elliptical contours. The cooling effect is felt over a larger area in the horizontal direction in contrast to the somewhat localized behavior seen at small gaps. Although the magnitude of the heat transfer coefficients is lower for the largest gap, the horizontal extent over which the influence of the fan is felt is greater.

Results for A=8.5 mm and the same three G/A values as above are shown along the second row of Fig. 6. Again, distinct cooling regimes are observed and seem to have the same dependence on G/A as at the larger amplitude, transitioning from lobed contours at small gaps, to circular contours at intermediate gaps, and finally to elliptical contours at large gaps. A further decrease of amplitude (to A=7.5 mm) results in the distributions shown along the third row of Fig. 6, and show a similar trend. However it is interesting to observe the small differences in contours for G/A=2.0 between the three largest amplitudes. Although the behavior is similar in all three cases, a departure from elliptical behavior begins to appear as the amplitude decreases. A secondary pattern starts to form at the two extreme edges of the elliptical contours, forming two,
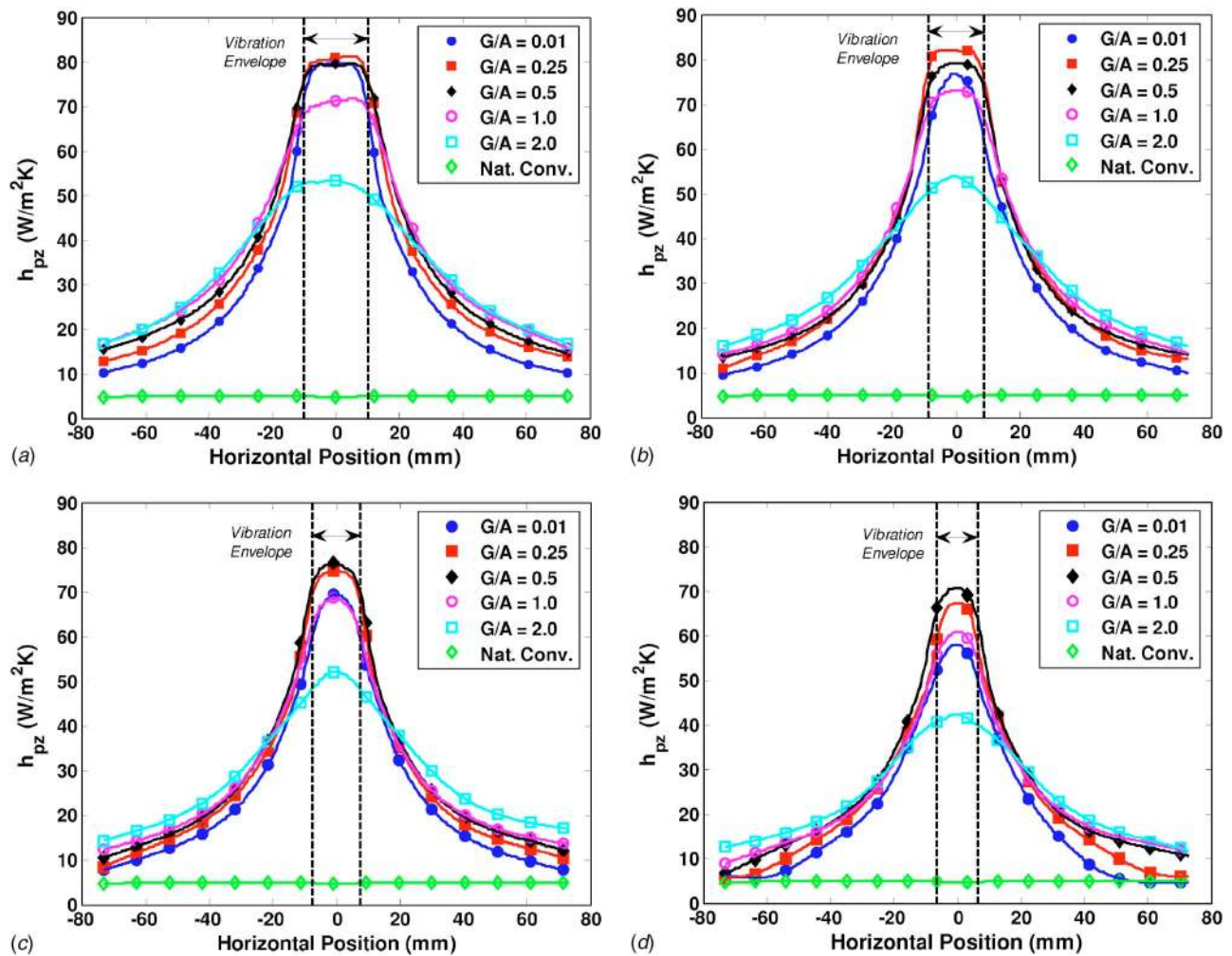
Fig. 7 Convection coefficient (h_{pz}) along horizontal direction ($y=0$) over range of nondimensional gaps (G/A $=0.01, 0.25, 0.5, 1.0, 2.0$) for: (*a*) $A=10$ mm, (*b*) $A=8.5$ mm, (*c*) $A=7.5$ mm, and (*d*) $A=6.35$ mm. For comparison, the natural convection profile is also shown.

slightly larger circular patterns. This suggests that although similar behavior is observed for different amplitudes at a given G/A, this behavior is slowly altered as the amplitude decreases.

This is even more apparent at the smallest amplitude (A $=6.35$ mm) as shown along the bottom row of Fig. 6. Notable differences relative to the larger amplitudes are seen at both the smallest and largest gaps. For $G/A=0.01$, the four distinct lobes observed at the higher amplitudes are now reduced to two, and the elliptical patterns typically seen at $G/A=2.0$ are also significantly altered. The regions with the greatest cooling are seen to have shifted from the stagnation region to just beyond the vibration envelope on either side. This is consistent with the observations in the literature regarding the fluid domain around a vibrating cantilever at small amplitudes [1], where vortices are shed as the fan tip passes the point of zero displacement and travel downstream. The heat transfer results suggest that these vortices are starting to form and impinge on the heater surface to create the observed areas of cooling on either side of the fan envelope. Previous results [16] showed that a further increase in G/A at small amplitudes ($G/A=4$, $A=5$ mm) generates two separate circular surface temperature contours on either side of the fan envelope, with very little cooling in the stagnation region. It appears that the reason for the differences observed in behavior between large and small amplitudes could be due to a change in flow/heat transfer regime. It is interesting to note that for various types of fluid flow including internal, external, and free streams, Bejan [18] has suggested that

the *local* Reynolds number at which transition from laminar to turbulent flow occurs is of the order 10^2, regardless of the type of flow considered. The local Reynolds number (Re_l) for a vibrating cantilever can be defined as:

$$Re_l = \frac{V_{rms}A}{\nu} \qquad (7)$$

It is interesting to compare the magnitude of Re_l for the two smallest amplitudes, which is 680 and 940 for $A=6.35$ and 7.5 mm, respectively. As the magnitude of Re_l changes from the order of $10^2 – 10^3$, a transition would therefore be expected as is the case with the experimental observations. The area-averaged trends of heat transfer performance also suggest a change in regime, as will be shown in subsequent sections.

Temperature traces along the horizontal centerlines of the heater surface are analyzed next. These are shown for $A=10$, 8.5, 7.5, and 6.35 mm in Figs. 7(*a*)–7(*d*), respectively. Each plot includes five nondimensional gaps ranging from $G/A=0.01$ to 2.0 as well as the corresponding natural convection distribution for comparison. Also illustrated by two vertical dashed lines is the horizontal extent of the vibration envelope, decreasing in size as the amplitude is reduced. A number of important trends can be observed from this data. In general, the heat transfer coefficient near the stagnation region (within the vibration envelope) is nearly uniform, and drops in value beyond this region. The steep-

ness of this drop is dependent on the gap, with the steepest drop occurring at the smallest gap. Although the magnitude of convection coefficient is obviously different for the two extreme gaps ($G/A = 0.01$ and 2.0), a more localized cooling zone is observed at smaller gaps in general, whereas the temperature profile flattens at large gaps. At small gaps, the fluid motion has limited physical space to diffuse before contacting the heat source, causing the observed localized cooling effect. Also inferred from these plots is the existence of an optimal gap that yields the highest stagnation-region heat transfer. At the largest amplitude (Fig. 7(a)), for example, the highest stagnation performance occurs for $G/A = 0.25$, and decreases beyond $G/A = 0.5$. For $A = 8.5$ mm (Fig. 7(b)), the optimum gap is more distinct, with the maximum convection coefficients being 76.7, 82.0, and 79.2 W/m² K for $G/A = 0.01$, 0.25, and 0.5, respectively. As the amplitude is decreased to $A = 7.5$ mm (Fig. 7(c)), the optimal gap is seen to occur at a larger G/A, where the maximum h_{pz} values are 69.3, 74.3, 76.4, and 68.6 W/m² K for $G/A = 0.01$, 0.25, 0.50, and 1.0, respectively. Similar results are observed for an amplitude of $A = 6.35$ mm (Fig. 7(d)), where the maximum performance is 57.8, 67.2, 70.8, and 60.8 W/m² K for $G/A = 0.01$, 0.25, 0.50, and 1.0, respectively. It is interesting to note that for this amplitude, the performance for a gap as large as $G/A = 1.0$ is better than the closest gap. Data from the two larger amplitudes ($A = 10$ and 8.5 mm) suggest an optimal gap of $G/A \approx 0.25$, whereas for the two smaller amplitudes ($A = 7.5$ and 6.35 mm), $G/A \approx 0.5$ appears to be the optimum. Relative to the closest gap, the benefit of operating at the optimum gap for the four cases shown in Fig. 7 ranges from only 2% at $A = 10$ mm to over 20% at $A = 6.35$ mm. A more detailed treatment of stagnation behavior follows in the next section.

Predictive Correlations for Thermal Performance of Piezoelectric Fans

In order to generalize the heat transfer performance obtained from the experiments, correlations are developed based on the key parameters involved. A number of similarities may be identified between the behavior of piezoelectric fans and impinging jets. Factors such as jet diameter, jet velocity, and spacing from the target are analogous to vibration amplitude, tip velocity, and gap distance, respectively. Although the flow generated by the oscillating piezoelectric fans is inherently unsteady, the results presented in this work are time-averaged convection coefficients. The heat transfer coefficient with piezofans is therefore expected to correlate with these parameters in a form similar to that in jet impingement. In the following, the applicable nondimensional parameters are first defined and predictive correlations then proposed.

Nondimensional Parameters. The appropriate length scale for the local Nusselt number is chosen to include both the vibration amplitude and fan width by employing the hydraulic diameter (D_{pz}) of the vibration envelope expressed as

$$D_{pz} = \frac{4Aw}{2A + w} \quad (8)$$

This is also consistent with the length scale used for noncircular impinging jets, and captures important behavior expected at the two extremes of $A \ll w$ and $A \gg w$. For the former extreme where a very wide fan is used $D_{pz} \approx 4A$, and one would expect amplitude to be the dominant factor in describing heat transfer performance. In other words, an increase in width would not affect the magnitude of the local performance. The latter extreme would be realized for very thin fans with $D_{pz} \approx 2w$. An increase in amplitude in this case would not have as great an effect on the fluid motion as would an increase in width. The local and area-averaged Nusselt numbers (Nu and $\overline{\text{Nu}}$) are given as

$$\text{Nu} = \frac{h_{pz}D_{pz}}{k}, \quad \overline{\text{Nu}} = \frac{\overline{h}_{pz}D_{pz}}{k} \quad (9)$$

where $\overline{h}_{pz}$ is determined from the size of an arbitrary heat source and is given as

$$\overline{h}_{pz} = \frac{1}{A_{eq}} \int_{A_{eq}} \int h_{pz} dA_{eq} \quad (10)$$

where A_{eq} is the area of the heat source. The stagnation Nusselt number (Nu_0) is the local Nusselt number at the geometric center of the vibration envelope which is based on the convection coefficient at that location (h_0) and is expressed as

$$\text{Nu}_0 = \frac{h_0 D_{pz}}{k} \quad (11)$$

The Reynolds number for piezoelectric fans (Re_{pz}) is given below and is defined using the maximum tip velocity of the fan, or the product of frequency and amplitude (ωA), the kinematic viscosity (ν) of the working fluid, and the same length scale chosen for Nu:

$$\text{Re}_{pz} = \frac{\omega A D_{pz}}{\nu} \quad (12)$$

Although the vibration amplitude appears in both Nu and Re_{pz}, a change in amplitude is manifested to a larger extent in Re_{pz} due to its direct influence in both the magnitude of tip velocity and hydraulic diameter. Nominal Re_{pz} values for the four amplitudes considered are 3550, 2810, 2370, and 1860 for $A = 10$, 8.5, 7.5, and 6.35 mm, respectively.

Area-Averaged Nusselt Number. At small gaps the temperature contours indicate symmetric behavior in the horizontal and vertical directions, whereas at large gaps, better cooling is noticed in the horizontal direction. Thus, the optimum conditions for cooling appear to be strongly tied to the target area over which the heat transfer is averaged; different target area definitions could result in different optimal conditions. From the results obtained in this work, it was found that averaging over a square- and circular-shaped target area agreed to within 1–2% as long as the averaging area was identical; thus all the results in the following are area averaged over a circular area with a diameter of D_{eq}. The impact of increasing the diameter over which the heat transfer coefficient is averaged (by considering a larger subset of pixels within the thermal image) is illustrated in Fig. 8 for the largest amplitude $\text{Re}_{pz} = 3550$ over a range of gaps. The heater size is represented in terms of a nondimensional diameter (D_{eq}/A), where a value of 2 denotes a heater size with its diameter just inscribed within the horizontal extent of the vibration envelope. The area-averaged Nusselt number is approximately equal to the stagnation value for $D_{eq}/A < 1$; well beyond this region ($D_{eq}/A > 3$), the behavior transitions to an exponential decay. This type of behavior is comparable to that seen in jet impingement studies [19,20]. Correlations in the current work are thus based on the forms of the equations used in jet impingement studies [14,21] to account for the behavior at the two extremes and the transition in between:

$$\overline{\text{Nu}} = \text{Nu}_0(1 + [a \exp\{b(D_{eq}/A)\}]^{-P})^{-1/P} \quad (13)$$

where a, b, and P are taken as variable parameters to be determined from a regression analysis. When the coefficient b takes a negative value, the appropriate behavior is captured for both small and large D_{eq}/A values.

The behavior of the average Nusselt number normalized with the stagnation-region value ($\overline{\text{Nu}}/\text{Nu}_0$) is compared for all four Re_{pz} (i.e., amplitudes) in Figs. 9(a) and 9(b) at the smallest ($G/A = 0.01$) and largest ($G/A = 2.0$) gaps, respectively. For $G/A = 0.01$, the exponential decay observed for $D_{eq}/A > 3$ seems to transition to a linear decay as Re_{pz} is decreased. The curvature
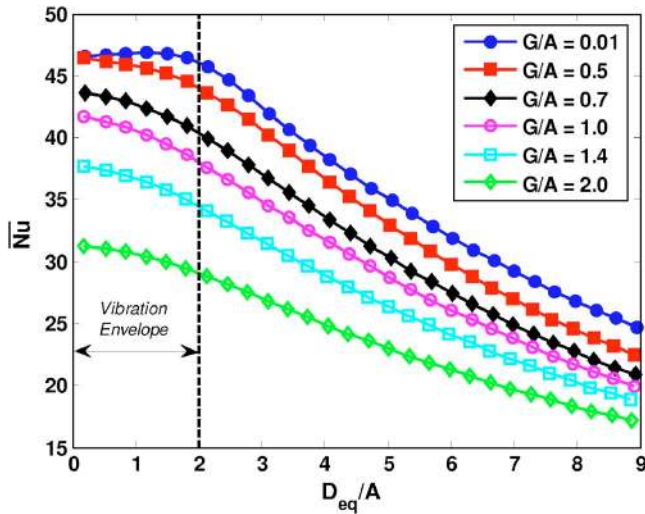
Fig. 8 Area-averaged Nusselt number ($\overline{Nu}$) versus nondimensional diameter of circular heater (D_{eq}/A) for $Re_{pz}=3550$ ($A=10$ mm) over range of nondimensional gaps ($G/A=0.01-2.0$)

(second derivative) of the decay in this region is 0.007, 0.003, and 0.002 for $Re_{pz}=3550$, 2810, and 2370, respectively. The curvature then becomes negative (-0.002) at the smallest amplitude ($Re_{pz}=1860$). The transition from a four-lobe to a two-lobe pattern in the local heat transfer coefficient distributions in the first column of Fig. 6 are reflected in the results in Fig. 9 as well. For $G/A=2.0$ (Fig. 9(b)), the differences become more stark, where curves from the largest three Re_{pz} are nearly identical, but that for $Re_{pz}=1860$ exhibits a different behavior. Accordingly, results from the smallest Re_{pz} are not included in the correlations proposed in this work. However, the correlations developed can still be used for the smallest amplitude but would result in a somewhat greater deviation.

Stagnation Nusselt Number. The experimental stagnation Nusselt numbers for the three largest Re_{pz} are shown in Fig. 10 over the full range of gaps considered. A smooth fit is superimposed on each set of data to better reveal the trends. As observed earlier with the horizontal centerline profiles, the stagnation Nusselt number increases until an optimum G/A is reached, after which point, it decreases. For the largest amplitude ($Re_{pz}=3550$), the maximum Nu_0 occurs in the range of G/A between 0.1 and 0.2. As Re_{pz} is decreased, the maximum Nu_0 also decreases as is expected, but the corresponding optimum gap location increases. In contrast, the optimum spacing in the jet impingement literature has been suggested to be independent of Re_{pz}, with a value of $G/A \approx 10$ [15,19,20,22].

The size of the potential-core region (with an undisturbed velocity profile) in jets becomes smaller with increasing distance from the jet outlet, and disappears altogether at roughly five jet diameters, and is responsible for the independence of jet Reynolds number for the stagnation heat transfer. On the other hand, the velocity field is extremely complex for a vibrating cantilever [1,5,6] and its structure is highly dependent on the gap. The experimental trends suggest that when operating at the optimum gap, more of the energy of the excited fluid is used for cooling. The gap where this occurs is smaller for fluid of higher energy (large amplitudes) when compared to that of lower energy (small amplitudes). A rigorous analysis of the fluid domain at various gaps and amplitudes is underway to better understand the apparent trends of the optimal gap based on the underlying physics. The dependence of the optimum gap (G_{opt}) on Re_{pz} for the largest three Re_{pz} follows a power law relationship:
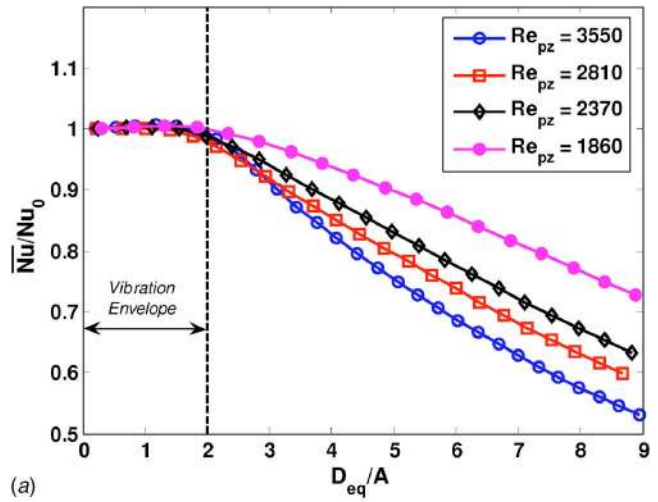
(a)
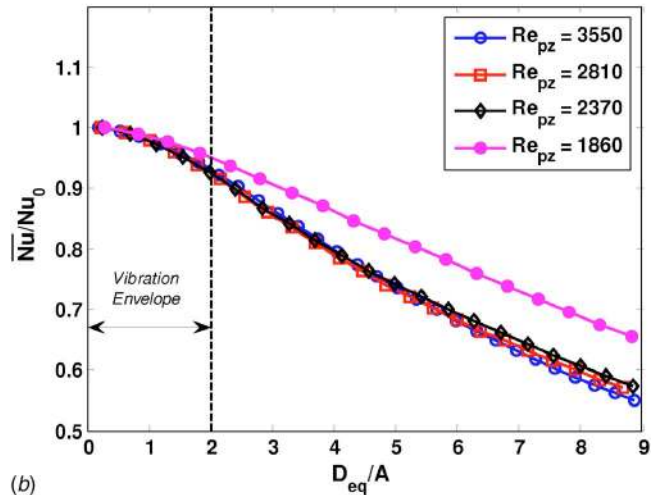
(b)

Fig. 9 Normalized area-averaged Nusselt numbers for four different Reynolds numbers ($Re_{pz}=3550$, 2810, 2370, and 1860 corresponding to $A=10$, 8.5, 7.5, and 6.35 mm, respectively) with (a) $G/A=0.01$ and (b) $G/A=2.0$

$$\frac{G_{opt}}{A} = 5.289\left(\frac{Re_{pz}}{1000}\right)^{-2.765} \qquad (14)$$

The stagnation Nusselt number Nu_0 is correlated to Re_{pz} and G/A using the form:

$$Nu_0 = (Re_{pz})^q\left[C_1\left(\frac{G}{A}\right)^r + C_2\right] \qquad (15)$$

where q, r, C_1, and C_2 are all considered variable parameters. The only modification introduced here relative to the form usually seen in jet impingement is the additional parameter (C_2), which accounts for the differences in the two flow situations. Only the region beyond the maximum ($G/A > G_{opt}/A$) is considered, consistent with jet impingement correlation efforts [22]; 48 experiments are included in the regression.

A least-squares approach was used to estimate the seven variable parameters in Eqs. (13) and (15), with the results listed in Table 2, yielding average and maximum deviations of 3.3% and 11.4%, respectively for the area-averaged Nusselt number. The quality of fit for the stagnation Nusselt number using Eq. (15) is illustrated in Fig. 11(a) where the correlation has average and maximum absolute deviations of 2.1% and 5.8%, respectively. The Reynolds number exponent (q) ranges between 0.39 and 0.47, which is comparable to those seen for jet impingement typically
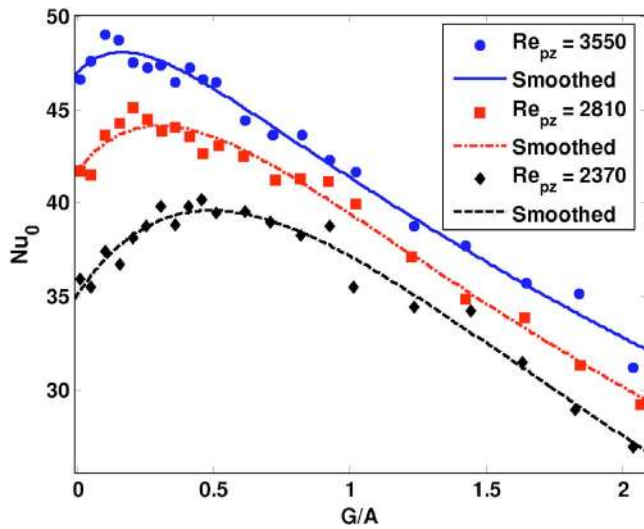
Fig. 10 Stagnation Nusselt number (Nu_0) behavior versus nondimensional gap (G/A) for three separate Reynolds numbers (Re_{pz}) corresponding to vibration amplitude of 10 mm ($Re_{pz}=3550$), 8.5 mm ($Re_{pz}=2810$), and 7.5 mm ($Re_{pz}=2370$)

between 0.3 and 0.5 [14]. The quality of fit for the average Nusselt number is found using the estimated stagnation Nusselt number from Eq. (15) as an input into Eq. (13); Fig. 11(*b*) shows that the correlation agrees quite well with the experimental data yielding average and maximum deviations of 3.3% and 11.4%. This correlation is valid for $G/A > G_{opt}/A$ (Eq. (14)) and for $2400 < Re_{pz} < 3500$ with the heater size $D_{eq}/A < 9$. The correlations can also be used for Re_{pz} as low as 1860 (the smallest amplitude considered); however the resulting accuracy is somewhat lower, yielding average and maximum deviations of 3.71% and 23.4%, respectively.

Conclusions

Local heat transfer coefficients are investigated for a single piezoelectric fan at various vibration amplitudes and gaps. The thermal maps exhibit a lobed-contour behavior at large gaps, transitioning to nearly circular (or rounded square) contours at intermediate gaps, and finally elliptical contours at small gaps. An optimal gap is noted both in the horizontal centerline profiles of local heat transfer coefficient and in the stagnation-region performance; the value of optimum gap is dependent on the vibration amplitude. Specifically, the optimum gap is small for large amplitudes and increases as the amplitude decreases. Predictive correlations are proposed for stagnation-region and area-averaged local Nusselt numbers. The experiments in this work were conducted with a single fan at a fixed fundamental resonance frequency, for

Table 2   Correlation coefficients from Eqs. (13) and (15) found from least squares analysis

Parameter	Value
a	1.132
b	−0.0899
P	25.13
q	0.440
r	1.451
C_1	−0.168
C_2	1.358
Average deviation (%)	3.3
Maximum deviation (%)	11.4
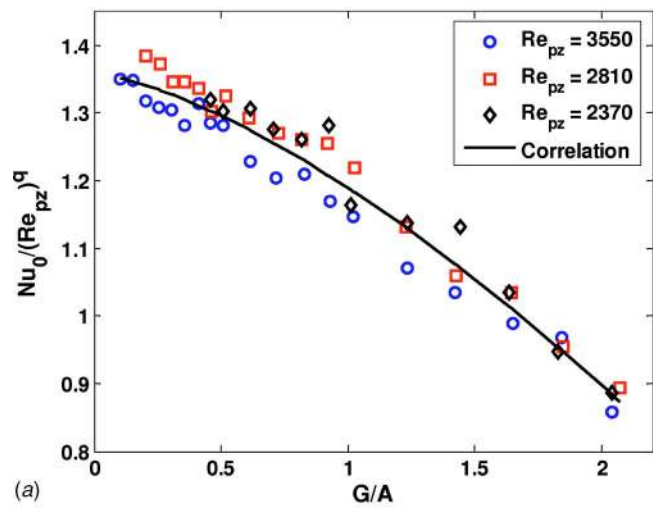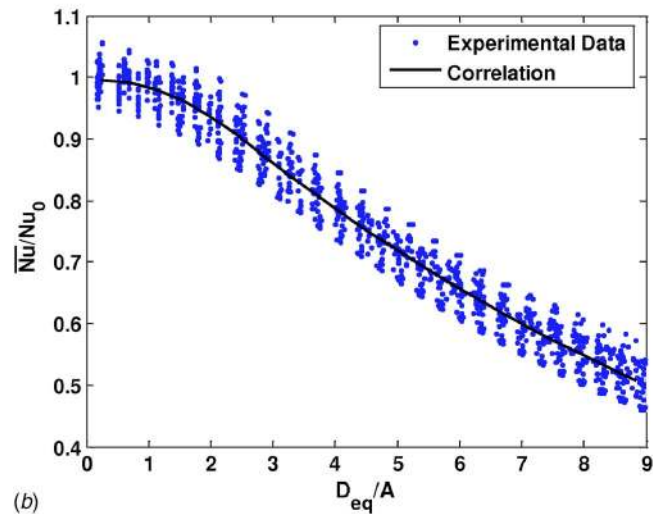
Fig. 11   Correlations with experimental data for (*a*) stagnation Nusselt number (Eq. (15)) with average and maximum deviations of 2.1% and 5.8%, respectively, and (*b*) area-averaged Nusselt number (Eq. (15) substituted in Eq. (13)) with average and maximum deviations of 3.3% and 11.4%, respectively

different amplitudes and fan tip to heat source gap distances. The applicability of the Reynolds number definition in this work in describing flow conditions at higher (or lower) frequencies remains to be verified. Additional studies are currently underway to account for the additional factors not considered in this work such as the presence of additional fans, and the use of fans with different geometries and structural characteristics.

Acknowledgment

Nomenclature

A = vibration amplitude (1/2 of peak to peak amplitude)
A_{heat} = area of heat source
D_{eq} = diameter of equivalent heat source
D_{pz} = hydraulic diameter of vibration envelope
G = gap distance

$\bar{h}$ = area-averaged forced convection coefficient
h = local forced convection coefficient
h_0 = stagnation forced convection coefficient
I_s = current from power supply
L = piezoelectric fan length
$\overline{\mathrm{Nu}}$ = area-averaged Nusselt number
Nu = local Nusselt number
Nu_0 = stagnation Nusselt number
q'' = heat flux
Re_l = local Reynolds number
Re_{pz} = reynolds number for vibrating cantilever
T_s = surface temperature
T_∞ = ambient temperature
V_{rms} = root mean square velocity of fan tip
V_s = voltage drop across heater
w = piezoelectric fan width

Greek Symbols

ε = surface emissivity
ν = kinematic viscosity
σ = Stefan-Boltzmann constant
ω = vibration frequency

Subscripts

gen = energy generation
mix = mixed regime convection
nc = natural convection
pz = forced convection (under piezoelectric actuation)
rad = radiation

References

[1] Kim, Y., Wereley, S. T., and Chun, C., 2004, "Phase-Resolved Flow Field Produced by a Vibrating Cantilever Plate Between Two Endplates," Phys. Fluids, **16**(1), pp. 145–162.
[2] Açıkalın, T., Raman, A., and Garimella, S. V., 2003, "Two-Dimensional Streaming Flows Induced by Resonating, Thin Beams," J. Acoust. Soc. Am., **114**(4), pp. 1785–1795.
[3] Açıkalın, T., Wait, S. M., Garimella, S. V., and Raman, A., 2004, "Experimental Investigation of the Thermal Performance of Piezoelectric Fans," Heat Transfer Eng., **25**(1), pp. 4–14.
[4] Wait, S. M., Garimella, S. V., and Raman, A., 2007, "Piezoelectric Fans Using Higher Flexural Modes for Electronics Cooling Applications," IEEE Trans. Compon. Packag. Technol., **30**(1), pp. 119–128.
[5] Açıkalın, T., Garimella, S. V., Raman, A., and Petroski, J., "Characterization and Optimization of the Thermal Performance of Miniature Piezoelectric Fans," Int. J. Heat Fluid Flow (in press).
[6] Ihara, A., and Watanabe, H., 1994, "On the Flow Around Flexible Plates, Oscillating With Large Amplitude," J. Fluids Struct., **8**(6), pp. 601–619.
[7] Schmidt, R. R., 1994, "Local and Average Transfer Coefficients on a Vertical Surface Due to Convection From a Piezoelectric Fan," *International Society Conference on Thermal Phenomena*, Washington, D.C, pp. 41–49.
[8] Kimber, M., Garimella, S. V., and Raman, A., 2006, "An Experimental Study of Fluidic Coupling Between Multiple Piezoelectric Fans," *International Society Conference on Thermal Phenomena*, San Diego, CA, pp. 333–340.
[9] Bürmann, P., Raman, A., and Garimella, S. V., 2003, "Dynamics and Topology Optimization of Piezoelectric Fans," IEEE Trans. Compon. Packag. Technol., **25**(4), pp. 592–600.
[10] Basak, S., Raman, A., and Garimella, S. V., 2005, "Dynamic Response Optimization of Piezoelectrically Excited Thin Resonant Beams," ASME J. Vibr. Acoust., **127**, pp. 18–27.
[11] Kim, B., Rho, J., and Jung, H., 2005, "Optimal Design of Piezoelectric Cantilever Fan by Three-Dimensional Finite Element Analysis," KIEE International Transactions on Electrical Machinery and Energy Conversion Systems, **5-B**(1), pp. 90–94.
[12] NASA Jet Propulsion Laboratory Web Site, URL: http://masterweb.jpl.nasa.gov/reference/paints.htm
[13] Liu, X., Lienhard V, J. H., and Lombara, J. S., 1991, "Convective Heat Transfer by Impingement of Circular Liquid Jets," ASME J. Heat Transfer, **133**(3), pp. 571–582.
[14] Stevens, J., and Webb, B. W., 1991, "Local Heat Transfer Coefficients Under an Axisymmetric, Single-Phase Liquid Jet," ASME J. Heat Transfer, **113**(1), pp. 71–78.
[15] Incropera, F., and DeWitt, D., 2002, *Fundamentals of Heat and Mass Transfer*, 5th ed., Wiley, New York.
[16] Kimber, M., Garimella, S. V., and Raman, A., 2006, "Experimental Mapping of Local Heat Transfer Coefficients Under Multiple Piezoelectric Fans," ASME Paper No. IMECE2006–13922.
[17] Vliet, G. C., and Ross, D. C., 1975, "Turbulent Natural Convection on Upward and Downward Facing Inclined Constant Heat Flux Surfaces," ASME J. Heat Transfer, **97**(4), pp. 549–555.
[18] Bejan, A., 2004, *Convection Heat Transfer*, 3rd ed., Wiley, New York.
[19] Rice, R. A., and Garimella, S. V., 1995, "Confined and Submerged Liquid Jet Impingement Heat Transfer," ASME J. Heat Transfer, **117**(4), pp. 871–877.
[20] Garimella, S. V. and Schroeder, V. P., 2001, "Local Heat Transfer Distributions in Confined Multiple Air Jet Impingement," ASME J. Electron. Packag., **123**(3), pp. 165–172.
[21] Churchill, S. W., and Usagi, R., 1972, "A General Expression for the Correlation of Rates of Transfer and Other Phenomenon," AIChE J., **18**(6), pp. 1121–1128.
[22] Sun, H., Ma, C. F., and Nakayama, W., 1993, "Local Characteristics of Convective Heat Transfer From Simulated Microelectronic Chips to Impinging Submerged Round Water Jets," ASME J. Electron. Packag., **115**, pp. 71–77.